Philosophical Magazine,
Vol. 86, No. 16, 1 June 2006, 2343–2358

Taylor & Francis
Taylor & Francis Group

Prediction of dislocation nucleation during nanoindentation of Al_3Mg by the orbital-free density functional theory local quasicontinuum method

ROBIN L. HAYES†, GREGORY HO‡, MICHAEL ORTIZ§ and EMILY A. CARTER*¶

†Department of Chemistry, New York University, New York, NY 10003-6688
‡Department of Chemistry, Princeton University, Princeton, NJ 08544
§Graduate Aeronautical Laboratories, California Institute of Technology, Pasadena, CA 91125
¶Department of Mechanical and Aerospace Engineering and Program in Applied and Computational Mathematics, Engineering Quadrangle, Princeton University, Princeton, NJ 08544-5263

(*Received 5 October 2005; in final form 6 December 2005*)

The first-principles prediction of dislocation nucleation in metallic systems subject to realistically sized indenters requires a multiscale approach due to the prohibitive computational expense. The largest empirical atomistic simulations include at most a billion atoms, at the same time requiring the parameterization of new interactions whenever an additional species or crystal structure is added. The multiscale orbital-free density functional theory–local quasicontinuum (OFDFT-LQC) method overcomes these problems by using first-principles OFDFT to capture the atomic interactions while relying upon LQC to evolve the macroscopic system. We use this method to indent the (111) surface of a $2 \times 2 \times 1\,\mu m$ piece of $L1_2\,Al_3Mg$. Using a localization criterion, the first dislocation is predicted to form off-axis on the $(1\bar{1}\bar{1})$ slip plane in the $[01\bar{1}]$ direction after the indenter has penetrated 70 nm. Other popular dislocation nucleation criteria give different predictions. These results are strikingly similar to those for indentation into the (111) surface of Al, indicating that the underlying crystal structure, not the atomic identity, is the most important factor in determining the onset of plasticity.

1. Introduction

Aluminium–magnesium alloys comprise an important class of structural materials used in the manufacturing of airplanes and cars. Precipitate hardening significantly alters the strength and long-term functionality of these materials. Although highly scrutinized, a complete understanding of the atomistic origin of precipitate formation and the resulting activated failure mechanisms is only starting to emerge for

*Corresponding author. Email: eac@princeton.edu

Philosophical Magazine
ISSN 1478–6435 print/ISSN 1478–6443 online
http://www.tandf.co.uk/journals
DOI: 10.1080/14786430500525829

these complex, multicomponent systems [1, 2]. Experiments generally agree that at room temperature precipitates appear in the following order:

$$\text{solid solution} \rightarrow \text{GP zones} \rightarrow \beta'' \rightarrow \beta' \rightarrow \beta. \quad (1)$$

The β'' particles are metastable $L1_2$ Al_3Mg particles believed to form from GP zones. These precipitates form coherent interfaces with the surrounding Al matrix [3]. Since the GP zones do not require the presence of vacancies to nucleate [4], it is unlikely that the β'' particles do either. By contrast, a variety of experimental techniques suggest that β' (approximate composition Al_3Mg_2) and β (α-Mn Al_3Mg_2) particles precipitate preferentially along grain boundaries [5], independently of GP zones and β'' particles [6]. Although the precipitate sequence does not change, plastic deformation does increase the number of particles formed [7]. The addition of different atomic species further complicates the precipitate behaviour [8]. For instance, under natural ageing conditions the addition of small amounts of Ag to a Al-10%Mg solution enhances the precipitation of finely dispersed precipitates of $L1_2$ Al_3Mg [9]. The present study seeks to characterize how dislocations form in the β'' phase during indentation and to compare its mechanical response to pure Al.

Identifying the spatial location and character of the first nucleated dislocation is a non-trivial task in macroscopic-sized materials. Dislocations typically occur in the middle of the solid so that *in situ* monitoring is often not possible [10, 11]. Dislocations move, so that later analysis usually fails to identify the position and character of the initial dislocation [12]. While characterizing the initial dislocation is easy for computational simulations, other equally challenging problems must be surmounted. Either the computational expense for first-principles calculations introduces finite size effects due to the small sample that must be studied [13] or empirical interactions must be tailored to each system [14–16], compromising transferability between systems and reliability of the predicted results. The multiscale orbital-free density functional theory–local quasicontinuum (OFDFT-LQC) method captures the best of both methodologies by incorporating atomic interactions from first-principles OFDFT [17] calculations into the LQC method [18–22]. In practice, instead of empirical-based constitutive relations, LQC uses the energies and stress tensors calculated directly with OFDFT.

Our previous work used OFDFT-LQC and the embedded atom method (EAM)-LQC to determine the initial dislocation nucleation character during indentation into pure fcc Al [23, 24]. OFDFT-LQC predicted dislocations would nucleate below the indenter, consistent with expectations for indentation into an atomically smooth surface with a spherical indenter. By contrast, the empirical EAM-LQC predicted dislocations would nucleate on the indenter surface, hinting that the EAM description may not be adequate. In this study, we consider $L1_2$ Al_3Mg, which is based on the same four-atom fcc lattice, but with one Al replaced by a Mg. This change will enable us to gauge the importance of atomic identity relative to the underlying crystal structure during the initial stages of dislocation nucleation. The primary goals of this study are twofold: to show that the OFDFT-LQC method can be extended to alloys and to explore the relative significance of crystal form vs. atomic identity during dislocation nucleation.

2. Methods

2.1. *Indentation setup*

In order to optimize comparisons between our previous work on Al and this work on Al_3Mg, identical simulation parameters are chosen wherever possible. Our 3D $2\,\mu m \times 2\,\mu m \times 1\,\mu m$ tetragonal LQC mesh, used to represent a bulk sample of Al_3Mg, is composed of 210 ten-node tetrahedral elements each with four quadrature points. Each quadrature point requires a separate OFDFT calculation of the energy and stress. The crystal is oriented such that the x-axis, y-axis, and z-axis coincide with the $[\bar{1}10]$, $[\bar{1}\bar{1}2]$, and [111] directions, respectively. The (111) surface starts at $z = 0$. In this orientation, a mirror plane passes through $x = 0$, so that only half of the mesh needs to be considered, thereby halving the computational expense. A simple energy penalty is used to enforce the position of the surface nodes at each step during the indentation [24]. The Cauchy–Born approximation means that there is no inherent length scale to LQC, as long as the quadrature points are sufficiently isolated from each other (i.e. a few angstroms). Hence, any length scale can be arbitrarily set. Unlike fully atomistic simulations which are restricted to tip sizes of the order of 10 nm, we can fix our length scale to reproduce any size indenter. In the absence of direct experiments for this system, we choose a length scale that results in a hard 750 nm spherical indenter, the same length scale used in our previous Al work. This value is at the upper end of the size range often used in indentation experiments, but could easily be scaled to smaller indenter tips and bulk sample sizes.

The nature of OFDFT-LQC imposes two constraints on the simulations. First, since the energy and stress tensor are calculated from quantum mechanics in the absence of a classical thermostat, the simulation is effectively at 0 K. A recent extension of the quasicontinuum method accounts for finite temperature [25], providing a means to lift this restriction in future studies. Second, unlike the non-local quasicontinuum method, there is no mechanism to resolve the mesh down to individual atoms. Although possible in theory, this awaits a method to eliminate periodic images inherent in the current reciprocal-space implementation of OFDFT through either screening or a real-space OFDFT scheme. Consequently, the simulation cannot accommodate an atomistic representation of dislocations, and hence must be stopped as soon as a dislocation is predicted to form, since further simulation will not exhibit the correct mechanical response.

$L1_2$ crystals are known to have active octahedral slip systems ($\{111\}$ slip planes in the $\langle 110 \rangle$ directions) at low temperatures with cubic slip systems ($\{100\}$ slip planes in the $\langle 110 \rangle$ directions) becoming active at higher temperatures [26–29]. Like fcc crystals, the $\langle 110 \rangle$ directions may be split into Shockley partials of $\langle 112 \rangle$ character. All of these easy slip systems will be considered here.

2.2. *Validation of OFDFT-LQC*

Density functional theory (DFT) is the current method of choice for accurate, first-principles predictions of materials properties. However, the LQC method requires that the underlying DFT method be evaluated millions of times during the course of an indentation simulation. Hence, the particular implementation of the DFT method must be exceptionally rapid. Traditional Kohn–Sham (KS)-DFT scales as $O[N^3]$ due

to orthogonalization of the orbitals. Furthermore, k-point sampling in metallic systems often increases the expense by a factor of 1000. Consequently, KSDFT is prohibitively expensive for use in LQC indentation simulations. Orbital-Free (OF)-DFT provides a linear scaling $O[N\ln(N)]$ alternative since the density is optimized directly, without the need for orbitals or k-points. The trade-off is accuracy. Without orbitals, the kinetic energy contribution to the total energy is only known in certain limits and purely local ion–electron pseudopotentials (used to represent the valence electron interaction with the nuclei plus core electrons) must be employed. The development of accurate kinetic energy functionals is still an active area of research. The current functionals work well for nearly free-electron materials such as main group metals. Recently, a method for creating local pseudopotentials that reproduce accurate non-local pseudopotential results for materials with more localized electron distributions has been developed [30]. However, local pseudopotentials for Al and Mg have not yet been constructed with this method. Therefore it should be possible to improve the accuracy of the present simulations when these improved pseudopotentials become available. Given these anticipated handicaps, the OFDFT-derived material properties of a given system must be carefully validated against experimental data and KSDFT predictions prior to the use of OFDFT in the computer-intensive indentation simulations.

The OFDFT calculations [17] employed the commonly used Goodwin–Needs–Heine (GNH) local pseudopotential [31] for aluminium and an OFDFT-derived local pseudopotential [32] for magnesium, the local density approximation (LDA) for the treatment of electron exchange and correlation [33, 34], and a converged kinetic energy cutoff (E_{cut}) of 60 Rydberg. The corresponding KSDFT calculations used the CASTEP code [35] with the same local pseudopotentials, a converged kinetic energy cutoff of 44 Rydberg, and a symmetry-reduced $20 \times 20 \times 20$ Monkhorst–Pack k-point sampling grid. Finite basis set corrections extrapolated from $dE_{\text{tot}}/d\log(E_{\text{cut}})$ were only applied to the stress tensor in the KSDFT resolved shear stress calculations. Consequently, the differences between OFDFT and KSDFT with local pseudopotentials arise solely from the kinetic energy density functional.

A detailed comparison of EAM vs. OFDFT Al properties was presented previously [24]. Although EAM matched some of the experimental data better, the relative ordering of stacking fault vs. twinning energies, the resolved shear stress curve, and the physically reasonable location of initial dislocations indicate that OFDFT may provide a superior description. Table 1 lists the material properties of Al_3Mg for OFDFT vs. KSDFT and experiment. Since $L1_2$ Al_3Mg is metastable, and only exists as small precipitates in an aluminium matrix, direct measurements of its material properties are exceedingly difficult to obtain. The experimental equilibrium lattice constant is estimated from a linear interpolation between bulk fcc aluminium and a dilute aluminium–magnesium alloy. KSDFT with a non-local pseudopotential underestimates the lattice constant, as expected in LDA calculations. KSDFT with the local pseudopotentials does better, but this should be considered fortuitous, since the less flexible local potential should yield results no better than a similarly constructed non-local potential. Here the local pseudopotentials are constructed in entirely different manners from the non-local pseudopotentials, leading to accidentally superior behaviour.

Table 1. Comparison of lattice spacing, a_{eq}, bulk modulus, B, and elastic constants, C_{ij}, from OFDFT (this work), KSDFT, and experimental results.

Method	a_{eq} (Å)	B (GPa)	C_{11} (GPa)	C_{12} (GPa)	C_{44} (GPa)
OFDFT (WT)	4.15	53.5	69	46	18
OFDFT (WGC)	4.15	53.1	69	45	17
OFDFT (dd-WGC)	4.12	59.5	79	50	34
KSDFT (local)	4.12	58.1	106	69	21
KSDFT (non-local) [2]	4.05	70.6			
Experimental [54]	4.15				

Since OFDFT is an approximation to KSDFT, the appropriate comparison is not to experiment but instead to KSDFT employing the same local pseudopotentials as used in the OFDFT calculations. This comparison is made below. In addition to the choice of local pseudopotential, an OFDFT calculation is defined by the choice of kinetic energy density functional (KEDF). Three different KEDFs were tested here for OFDFT. The general form for density-independent linear response kinetic energy functionals, $T^{\alpha\beta}$, is

$$T^{\alpha\beta} = C_{\mathrm{TF}}\left\langle \rho^{\alpha}(\vec{r}) \middle| w_{\alpha\beta}\left[\left|\vec{r}-\vec{r}'\right|\right] \middle| \rho^{\beta}(\vec{r}')\right\rangle \tag{2}$$

where ρ is the density, and $w_{\alpha\beta}$ is the kernel. The simplest version due to Wang and Teter (WT) [36] sets $\alpha = \beta = 5/6$. A slightly more complicated form due to Wang, Govind and Carter (WGC) [37] finds optimal parameters of $\alpha = (5+\sqrt{5})/6$ and $\beta = (5-\sqrt{5})/6$. The third, also due to Wang, Govind and Carter (dd-WGC) [38], substitutes a density-dependent kernel, $w_{\alpha\beta}[\zeta_{\gamma}(\vec{r},\vec{r}'), |\vec{r}-\vec{r}'|]$, where

$$\zeta_{\gamma}(\vec{r},\vec{r}') = \left(\frac{k_{\mathrm{F}}^{\gamma}(\vec{r}) + k_{\mathrm{F}}^{\gamma}(\vec{r}')}{2}\right)^{1/\gamma} \tag{3}$$

and the Fermi wavevector, $k_{\mathrm{F}}(\vec{r}) = [3\pi^2\rho(\vec{r})]^{1/3}$. They use the same α and β, and treat γ as an adjustable parameter, with a suggested value of 2.7 for nearly free-electron-like metals. The lattice constant, a_{eq}, bulk modulus, B, and elastic constants, C_{ij}, are nearly identical for WT and WGC, but differ from our gold standard given by KSDFT with the same local pseudopotentials. The density-dependent kinetic energy functional should provide superior results for systems where the electron density deviates slightly from nearly free electrons, i.e. where the density becomes somewhat localized. With the exception of C_{44}, dd-WGC does improve the results a small, but significant amount. Another study by Carling *et al*. [2] also found that only dd-WGC can reproduce the heat of formation for Al_3Mg, indicating that dd-WGC better captures its material properties. Therefore, the density-dependent kernel will be used for the remainder of the study. The coupling between OFDFT and LQC requires the dd-WGC contribution to the stress tensor, which has not been derived previously. The derivation is included in the appendix.

The stress tensor plays a pivotal role. Not only is it used to update the LQC mesh via energy minimization based on atomic-level information, but it determines when a dislocation should form. Several theories on initial dislocation nucleation identify the maximum resolved shear stress along the available slip systems as the critical factor governing initial dislocation nucleation. For unstrained $L1_2$ systems, the $\langle 112 \rangle$ slip directions in the {111} planes are the lowest stress slip systems. In order to further validate our model, we compare the resolved shear stress in the $\langle 112 \rangle \{111\}$ slip system for OFDFT with the WT, WGC, and dd-WGC kinetic energy functionals and KSDFT using the same local pseudopotentials. The results, shown in figure 1, confirm that the OFDFT calculations reasonably reproduce the KSDFT results. The WT and density independent WGC kinetic energy functionals are nearly indistinguishable (dotted and dashed lines). The dd-WGC OFDFT results more closely follow the KSDFT results, particularly in the region where the distance between atoms becomes small. The strained system likely possesses less free-electron character, hence the dd-WGC kinetic energy functional provides a better description. The agreement between the dd-WGC OFDFT and the local pseudopotential KSDFT derived curvature near $\varepsilon = 0$ in figure 1 is better than the C_{44} agreement reported in table 1. The former measures the shear in the $\langle 112 \rangle$ direction when the z-axis is oriented along [111], while the latter measures the shear in the $\langle 010 \rangle$ direction when the z-axis is oriented along [001]. The (111) surface is more densely packed than the (100) surface, so the atomic neighbours are closer together than an equivalent strain in the [001] orientation. This probably means that the electron density is smoother in this configuration, and hence described slightly better by OFDFT than the corresponding OFDFT C_{44} calculation.

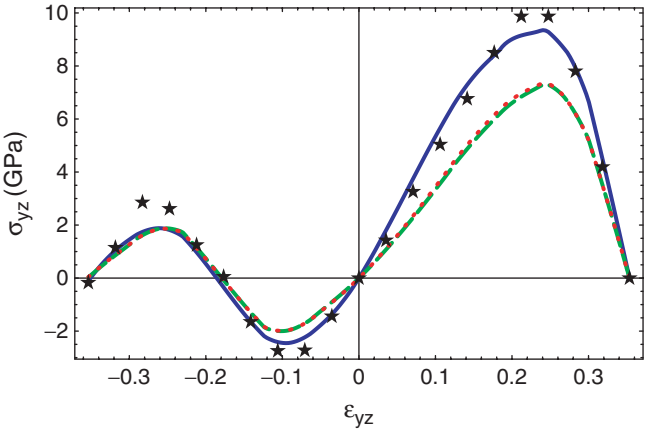

Figure 1. Resolved shear stress (RSS) along the $\langle 112 \rangle$ direction in the {111} slip plane. The OFDFT results for WT (red dot), WGC (green dash) and dd-WGC (solid blue) kinetic energy functionals are shown with the lines and the KSDFT (local pseudopotentials) results are marked with the stars. The overall agreement between OFDFT with the dd-WGC kinetic energy functional and KSDFT is reasonable.

2.3. *Localization criterion for dislocation nucleation*

The material tangent stiffness or acoustic tensor [39–44] has been a popular method to gauge the mechanical stability of a crystal. Like our previous work on Al [24], we express the stability factor as:

$$\Lambda = \sum_{i,J,k,L=1}^{3} C_{iJkL} N_J N_L k_i k_k \tag{4}$$

where $\boldsymbol{C}$ are the *mixed* material tangent moduli, $\boldsymbol{N}$ are the normals to the slip planes in the reference frame, and $\boldsymbol{k}$ are the slip directions (i.e. Burgers' vectors) in the deformed, spatial frame.

Whenever the minimum value of Λ, $\Lambda_{\min}$, becomes zero or negative, the crystal becomes unstable and a dislocation is predicted to form in the $\boldsymbol{N}$ slip plane in the $\boldsymbol{k}$ slip direction. Li *et al*. [44, 16] recently demonstrated a one-to-one correspondence between $\Lambda_{\min} = 0$ and the formation of dislocations in an embedded atom method molecular dynamics simulation. Rather than determining all the eigenvalues of the acoustic tensor at all the quadrature points at each indentation step, $\Lambda_{\min}$ is assigned to the smallest value of equation (4) evaluated for the six $\{100\}\langle 110\rangle$, twelve $\{111\}\langle 110\rangle$, and twelve $\{111\}\langle 112\rangle$ slip systems. This is equivalent to checking the known preferred perfect and partial dislocations for the $L1_2$ crystal structure.

3. Results

Figure 2 shows the load vs. displacement curve for indentation into the {111} surface. For comparison, results for Al are included from our previous work [24]. Since the OFDFT-LQC method cannot accommodate dislocations, the simulation must be

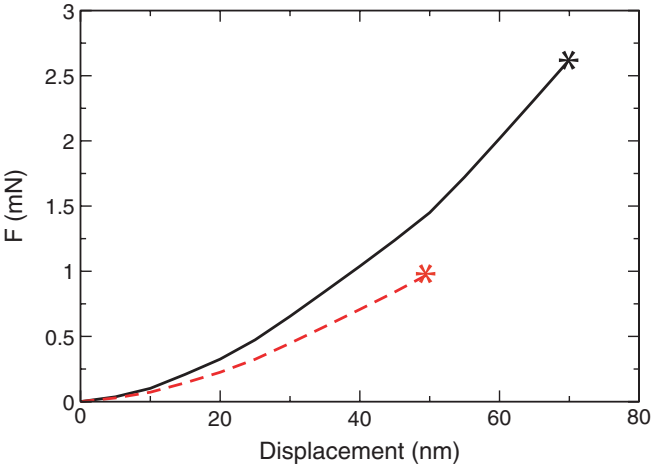

Figure 2. OFDFT-LQC load vs. displacement curve for indentation into the {111} surface of Al_3Mg (solid black line, this work) and Al (red dashed line, previous work [24]). The first dislocations occurs at a greater indentation depth and applied force in Al_3Mg than Al.

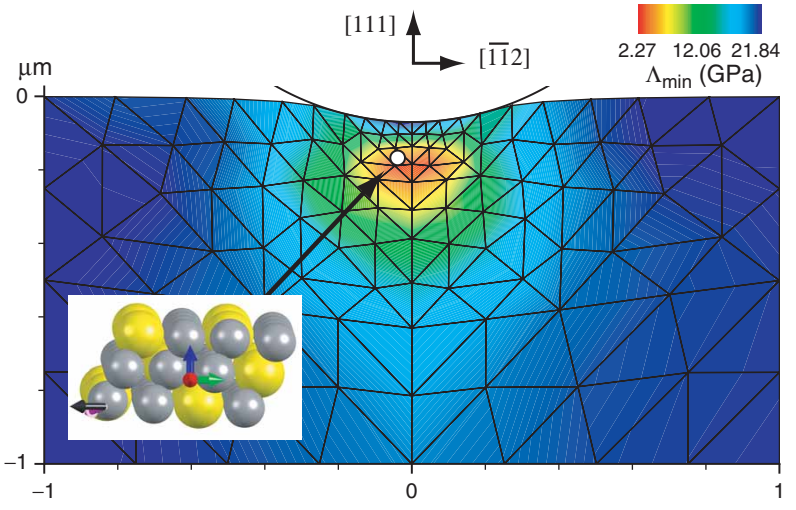

Figure 3. Contour plot in the $x = 0$ plane of the localization criterion after the indenter has penetrated 70 nm into the (111) Al_3Mg surface. The first dislocation is predicted to form ($\Lambda_{min} = 0$) off-axis and 168 Å beneath the surface. The location is projected onto the $x = 0$ plane and marked with a white dot. The inset shows the crystal structure (Al – grey, Mg – yellow), the *xyz* crystal orientation (red, green, blue arrows), the [1$\bar{1}\bar{1}$] slip plane normal (purple arrow), and the [01$\bar{1}$] slip direction (black arrow) for the dislocation that the localization criterion predicts will form.

stopped after the first dislocation is predicted to form via the localization criterion ($\Lambda_{min} = 0$). The '*' indicates where the first dislocation should form. In Al, this point is reached after the indenter has penetrated the surface 50 nm at a load of 0.98 mN, while in Al_3Mg the indenter must penetrate 70 nm and reach a load of 2.62 mN. Although $L1_2$ Al_3Mg is clearly more resistant to the initial formation of dislocations, the dislocation character is virtually identical to fcc Al; namely in both Al and Al_3Mg the dislocation is characterized by a [1$\bar{1}\bar{1}$] slip plane normal in the [01$\bar{1}$] direction. The {100}⟨110⟩ slip system is not preferred, at least at very low temperatures. Figure 3 shows a contour plot of the localization criteria on the $x = 0$ plane. The location of the initial dislocation, marked with a white dot, has been projected onto the *yz*-plane. This occurs off-axis ($x = -58$ nm, $y = -39$ nm) at a depth of 0.53 z/a, where z is the distance beneath the original surface and a is the radius of the spherical indenter in the *xy*-plane at the surface. This is very similar to what we found for Al nanoindentation, where the dislocation in Al also forms off-axis ($x = -59$ nm, $y = -39$ nm) at a depth of 0.56 z/a.

The striking similarity in the initial dislocation character strongly suggests that the primary factor dictating dislocation nucleation character and spatial location is the underlying crystal structure, not the atomic identity. Where the atomic identity expresses itself is the cost to initiate the dislocation. The larger load at a given indenter depth in Al_3Mg relative to Al is expected based on the Young's modulus in the [111] direction: 86 GPa for Al_3Mg, but only 55 GPa for Al, as calculated by OFDFT. Al_3Mg is expected to be a harder material, consistent with its exploitation in Al precipitate-hardening mechanisms. The atomic radius is probably the primary

factor determining the indenter depth required to nucleate a dislocation. The larger size of Mg (atomic radius = 1.45 Å, bond length in hcp ground state = 3.20 Å) relative to Al (atomic radius = 1.18 Å, bond length in fcc ground state = 2.86 Å) increases the barrier, and hence raises the required load that must be overcome before a dislocation can form. This is also evident in the OFDFT-calculated unstable stacking fault energy (without atomic relaxation): Al = 86 mJ/m^2 [24], Al_3Mg = 95 mJ/m^2. If this argument holds, then if Mg in the $L1_2$ crystal structure is replaced with species such as Si or B, which have smaller atomic radii than Al, we would predict that dislocations should form more easily.

The literature describes several other criteria with which to predict when dislocations will nucleate. Other methods include the maximum shear stress in the spirit of a simple Hertzian analysis, the maximum resolved shear stress, and some form of the strain. Figure 4 shows contour plots in the $x = 0$ plane of a variety of dislocation nucleation criteria. The predicted dislocation nucleation location is projected onto the $x = 0$ plane for the localization criterion (white dot) and the alternative criteria (purple dots). Figure 4(a) shows the maximum value of the principal shear stress calculated directly from the Cauchy stress tensor. In this case, the maximum value occurs off-axis on the indenter surface. If a simple Hertzian analysis [45] was correct, the maximum value of the principal shear stress would be directly beneath the indenter at a depth of approximately 0.51 z/a. The position predicted by the localization criterion (white dot) is actually closer to the Hertzian prediction than is the maximum shear stress prediction. Figure 4(b) plots the maximum value of the resolved shear stress (RSS) on any of the $\{100\}\langle 110\rangle$, $\{111\}\langle 110\rangle$, or $\{111\}\langle 112\rangle$ slip systems. Typically, a dislocation would be predicted to form if the RSS exceeds some critical value. In our simulation, the maximum RSS value occurs at the same spatial location as the maximum principal shear stress: on the indenter surface. Furthermore, the dislocation character does not match the localization criterion. The maximum RSS after the indenter has penetrated 70 nm is on the (010) plane in the [101] direction. Even at the unstable point predicted by the localization criterion (white point), the maximum RSS occurs on a different slip system, namely the (001) plane in the [110] direction. Figure 4(c) displays the contour plot of the von Mises stress given by

$$\sigma^{\text{Mises}} = \sqrt{\frac{(\sigma_{xx} - \sigma_{yy})^2 + (\sigma_{yy} - \sigma_{zz})^2 + (\sigma_{zz} - \sigma_{xx})^2 + 6(\sigma_{xy}^2 + \sigma_{yz}^2 + \sigma_{xz}^2)}{2}}. \quad (5)$$

Although not typically used to predict dislocation formation, the von Mises stress is often used as a general measure of the stress state of the system. The projection onto the $x = 0$ plane makes the maximum value of the von Mises stress (purple dot) appear close to the localization criterion (white dot). In reality they are 63 nm apart. Finally, figure 4(d) shows the von Mises strain given by

$$\varepsilon^{\text{Mises}} = \sqrt{\frac{(\varepsilon_{xx} - \varepsilon_{yy})^2 + (\varepsilon_{yy} - \varepsilon_{zz})^2 + (\varepsilon_{zz} - \varepsilon_{xx})^2 + 6(\varepsilon_{xy}^2 + \varepsilon_{yz}^2 + \varepsilon_{xz}^2)}{2}} \quad (6)$$

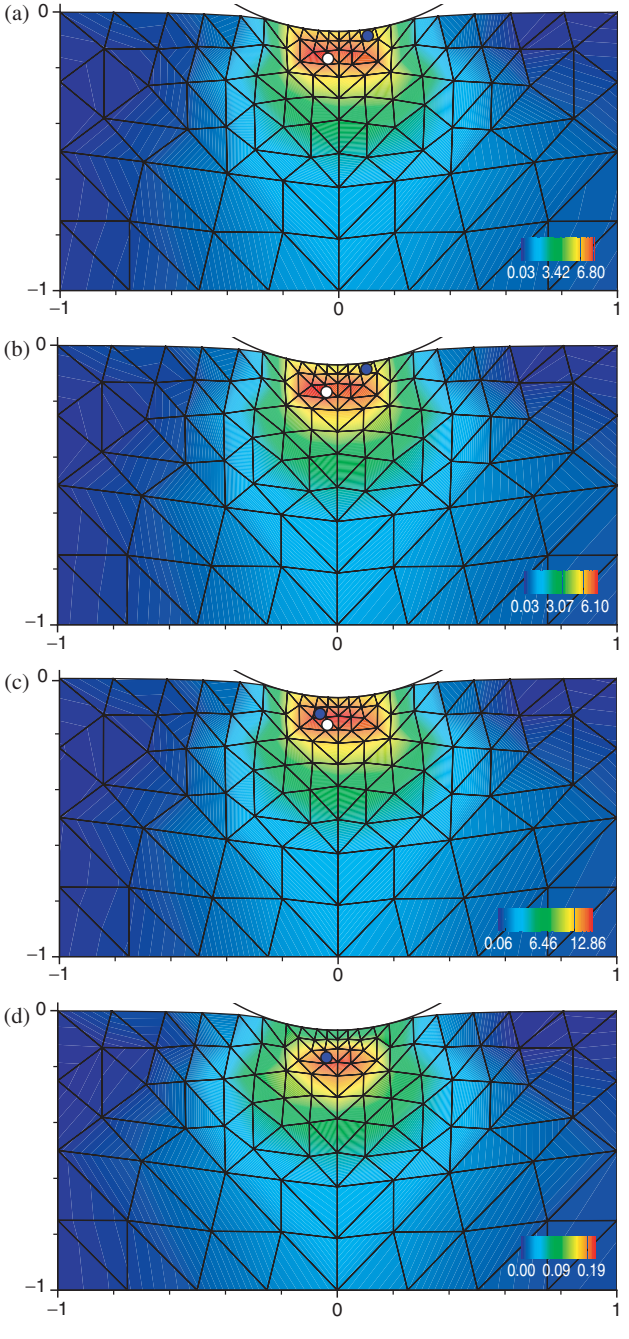

Figure 4. Contour plot of the (a) maximum shear, (b) RSS, (c) von Mises stress, and (d) von Mises strain, on the $x = 0$ plane when a dislocation is first predicted to form. The dislocation predicted by the localization criterion ($\Lambda_{\min} = 0$) is represented by a white circle projected onto the $x = 0$ plane. The purple circles mark where the dislocations are predicted to form according to the (a) maximum shear, (b) RSS, (c) von Mises stress, and (d) von Mises strain. Only the von Mises strain matches the dislocation predicted by the localization criterion.

where $\varepsilon \equiv (1/2)\log(\boldsymbol{C})$ is the logarithmic strain, defined in terms of the right Cauchy–Green deformation tensor $\boldsymbol{C} = \boldsymbol{F}^T\boldsymbol{F}$. Here, we approximate the logarithmic strain as $\varepsilon \approx (1/2)(\boldsymbol{C} - \boldsymbol{I})$. The maximum value of the von Mises strain exactly matches the localization criterion. None of these results are surprising. Our previous study on fcc Al [24] found nearly identical results. Namely, local deformations significantly alter the minimum stress that must be overcome before the first dislocation can form, resulting in the failure of either a Hertzian analysis or the critical resolved shear stress to correctly predict the qualitative character of the first dislocation. Other researchers have made similar observations. The strong sensitivity of the stress state to local deformations has been observed in Cu [46]. Moreover, small classical molecular dynamics simulations by Li *et al.* [47] have directly verified that the localization criterion correctly predicts where dislocations form.

4. Conclusions

OFDFT-LQC has proved amenable to the study of alloy systems with very little overhead required to incorporate multiple species. All the interactions between different species are automatically accounted for within DFT. The challenge lies in choosing a system that gives physically reasonable results within OFDFT. Compared to empirical potential methods whose parameters are fit to experimental data, the agreement with experimental bulk properties such as lattice constants and elastic constants may not be as good, but OFDFT has the advantage of automatically including the relevant physics without invoking ad hoc corrections or fitting a particular functional form. However, before OFDFT can be applied to a wide range of systems, more accurate kinetic energy functionals need to be developed.

At the atomistic level, $L1_2$ Al_3Mg behaves nearly identically to fcc Al, indicating that the local structure appears to be more important than the identity of the individual atoms, at least for the case of nearly free-electron metals. Further studies substituting other atoms such at Li or Na for Mg into the $L1_2$ crystal structure would clarify the universality of this behaviour. Several systems such as cubic diamond silicon [48] and $L1_2$ Pt_3Al [49] initially undergo phase transitions rather than dislocation nucleation. In theory, this could be incorporated into the OFDFT-LQC code, but at increased computational expense. Studying these systems, as well as others based on different crystal structures, would further delineate the respective roles of identity and structure in dislocation nucleation.

Acknowledgments

We are grateful to the US Department of Defense for support through Brown University's MURI Center for the 'Design and Testing of Materials by Computation: A MultiScale Approach', the US Department of Energy through Caltech's ASCI/ASAP Center for the Simulation of the Dynamic Response of Solids, and Accelrys for providing the CASTEP software.

Appendix A: Stress tensor contribution due to the Wang–Govind–Carter kinetic energy density functional

We calculate the Cauchy stress tensor with the following formula:

$$\sigma_{\alpha\beta} = \frac{1}{\Omega}\sum_{\upsilon}\frac{\partial E}{\partial h_{\alpha\upsilon}}h_{\beta\upsilon} \tag{A7}$$

where E is the total OFDFT energy, $\boldsymbol{h}$ is a matrix whose columns are the lattice vectors for a periodic unit cell, and Ω is the unit cell volume calculated from the determinant of $\boldsymbol{h}$. α, β, and υ are the spatial coordinates, $\{x, y, z\}$. Since the total OFDFT energy is a linear combination of ionic and electronic terms, we can calculate the stress contribution of each term separately. We only consider here the Wang–Govind–Carter kinetic energy density functional (WGC KEDF) term because the other terms have been published previously [50–52].

A.1. *The WGC KEDF contribution to the kinetic energy*

The energy of the Wang–Govind–Carter (WGC) kinetic energy density functional with a density-dependent kernel (dd-WGC) [38] is

$$T_{\mathrm{WGC}}^{\alpha'\beta'\gamma} = C_{\mathrm{TF}}\langle\rho^{\alpha'}(\vec{r})|w_{\alpha'\beta'}[\zeta_{\gamma}(\vec{r},\vec{r}'),|\vec{r}-\vec{r}'|]|\rho^{\beta'}(\vec{r}')\rangle \tag{A8}$$

where $\rho(\vec{r})$ is the electron density in real space,

$$C_{\mathrm{TF}} = \frac{3}{10}(3\pi^2)^{2/3}, \tag{A9}$$

the two-body Fermi wavevector

$$\zeta_{\gamma}(\vec{r},\vec{r}') = \left(\frac{k_{\mathrm{F}}^{\gamma}(\vec{r})+k_{\mathrm{F}}^{\gamma}(\vec{r}')}{2}\right)^{1/\gamma} \tag{A10}$$

and

$$k_{\mathrm{F}}(\vec{r}) = [3\pi^2\rho(\vec{r})]^{1/3}. \tag{A11}$$

The energy expression cannot be solved directly. Therefore, $w_{\alpha'\beta'}$ is Taylor expanded around a reference density, ρ_*, so that the expression can be evaluated in reciprocal space via fast Fourier transforms, which will be denoted by $\hat{F}$ throughout this section.

$$\begin{aligned} w_{\alpha'\beta'}[\zeta_{\gamma}(\vec{r},\vec{r}'),|\vec{r}-\vec{r}'|] = {} & w_{\alpha'\beta'} + w'_{\alpha'\beta'}\Theta(\vec{r}) + w'_{\alpha'\beta'}\Theta(\vec{r'}) + w''_{\alpha'\beta'_1}\frac{\Theta^2(\vec{r})}{2} \\ & + w''_{\alpha'\beta'_1}\frac{\Theta^2(\vec{r'})}{2} + w''_{\alpha'\beta'_2}\Theta(\vec{r})\Theta(\vec{r'}) \end{aligned} \tag{A12}$$

where

$$\Theta(\vec{r}) = \rho(\vec{r}) - \rho_*, \tag{A13}$$

$$k_{\mathrm{F}}^* = [3\pi^2\rho_*]^{1/3}, \tag{A14}$$

$$w_{\alpha'\beta'} = w_{\alpha'\beta'}(k_{\mathrm{F}}^*, |\vec{r} - \vec{r}'|), \tag{A15}$$

$$w'_{\alpha'\beta'} = \left.\frac{\partial w_{\alpha'\beta'}[\zeta_\gamma(\vec{r},\vec{r}'), |\vec{r} - \vec{r}'|]}{\partial\rho(\vec{r})}\right|_{\rho_*}, \tag{A16}$$

$$w''_{\alpha'\beta'_1} = \left.\frac{\partial^2 w_{\alpha'\beta'}[\zeta_\gamma(\vec{r},\vec{r}'), |\vec{r} - \vec{r}'|]}{\partial\rho^2(\vec{r})}\right|_{\rho_*}, \tag{A17}$$

$$w''_{\alpha'\beta'_2} = \left.\frac{\partial^2 w_{\alpha'\beta'}[\zeta_\gamma(\vec{r},\vec{r}'), |\vec{r} - \vec{r}'|]}{\partial\rho(\vec{r})\partial\rho(\vec{r}')}\right|_{\rho_*}, \tag{A18}$$

and

$$\widetilde{w}_{\alpha'\beta'} = \widehat{F}[w_{\alpha'\beta'}]. \tag{A19}$$

$\widetilde{w}_{\alpha'\beta'}$ is the solution to the following second-order differential equation, where the derivatives are with respect to $\eta_* = |\vec{g}|/(2k_{\mathrm{F}}^*)$.

$$\eta_*^2\widetilde{w}''_{\alpha'\beta'}(\eta_*, \rho_*) + [\gamma + 1 - 6(\alpha' + \beta')]\eta_*\widetilde{w}'_{\alpha'\beta'}(\eta_*, \rho_*)$$
$$+ 36\alpha'\beta'\widetilde{w}_{\alpha'\beta'}(\eta_*, \rho_*) = 20G(\eta_*)\rho_*^{5/3-(\alpha'+\beta')}, \tag{A20}$$

$$G(\eta_*) = f_{\mathrm{L}}^{-1}(\eta_*) - 3\eta_*^2 - 1, \tag{A21}$$

and f_{L}, the Lindhard function, is

$$f_{\mathrm{L}}(\eta_*) = \frac{1}{2} + \frac{1 - \eta_*^2}{4\eta_*}\ln\left|\frac{1 + \eta_*}{1 - \eta_*}\right|. \tag{A22}$$

Using the above solution, it is possible to obtain expressions for the Fourier transformation of all the terms in the Taylor expansion up to second order given in equation (A12).

$$\widehat{F}[w'_{\alpha'\beta'}] = -\frac{\eta_*\widetilde{w}'_{\alpha'\beta'}(\eta_*, \rho_*)}{6\rho_*} \tag{A23}$$

$$\widehat{F}[w''_{\alpha'\beta'_1}] = -\frac{\eta_*^2 \widetilde{w}''_{\alpha'\beta'}(\eta_*, \rho_*) + (7-\gamma)\eta_* \widetilde{w}'_{\alpha'\beta'}(\eta_*, \rho_*)}{36\rho_*^2} \tag{A24}$$

$$\widehat{F}[w''_{\alpha'\beta'_2}] = -\frac{\eta_*^2 \widetilde{w}''_{\alpha'\beta'}(\eta_*, \rho_*) + (1+\gamma)\eta_* \widetilde{w}'_{\alpha'\beta'}(\eta_*, \rho_*)}{36\rho_*^2} \tag{A25}$$

The values of α' and β' correspond to different kinetic energy density functionals. Wang, Govind and Carter [38] recommend using $\alpha' = (5+\sqrt{5})/6$ and $\beta' = (5-\sqrt{5})/6$ because this yields the correct limit for large $\vec{g}$-vectors. Given no other constraints, γ can then be varied to achieve properties that best agree with KSDFT, with 2.7 being the optimal value found for aluminium. Another value for γ was recently proposed for use in semiconductors [53]. The response kernel Taylor expansion of equation (A12) is thus evaluated in reciprocal space, by Fourier transforming each term of equation (A12).

A.2. *The stress tensor contribution from the dd-WGC KEDF*

The stress due to the Wang–Govind–Carter (WGC) kinetic energy density functional with a density-dependent kernel (dd-WGC) depends on whether ρ_* changes as the cell volume changes or if it is a fixed number. The results presented in this paper allowed the density to change with the volume, but both expressions are included here for completeness.

For the case that $\rho_* = N_e/\Omega$, where N_e is the total number of electrons,

$$\begin{aligned}\sigma_{\alpha\beta}^{\mathrm{WGC}} = \sum_{g\neq 0}\Bigg\{ & -\frac{1}{3}T_{\mathrm{WGC}}^{\alpha'\beta'\gamma}\delta_{\alpha\beta} + C_{\mathrm{TF}}\eta_*\left(\frac{g_\alpha g_\beta}{g^2} - \frac{1}{3}\delta_{\alpha\beta}\right) \\ & \times \left[\rho_{\alpha'}(-\vec{g})d_{00}\rho_{\beta'}(\vec{g}) + \rho_{\alpha'+1}(-\vec{g})d_{01}\rho_{\beta'}(\vec{g})\right. \\ & + \rho_{\alpha'}(-\vec{g})d_{01}\rho_{\beta'+1}(\vec{g}) + \rho_{\alpha'+2}(-\vec{g})d_{02}\rho_{\beta'}(\vec{g}) \\ & \left. + \rho_{\alpha'}(-\vec{g})d_{02}\rho_{\beta'+2}(\vec{g}) + \rho_{\alpha'+1}(-\vec{g})d_{11}\rho_{\beta'+1}(\vec{g})\right]\Bigg\}.\end{aligned} \tag{A26}$$

Here

$$\rho_D(\vec{g}) = \widehat{F}[\rho^D(\vec{r})], \tag{A27}$$

$$d_{00} = \frac{\partial\widehat{F}[w_{\alpha'\beta'}]}{\partial\eta_*} + 2\rho_*\frac{\partial\widehat{F}[w'_{\alpha'\beta'}]}{\partial\eta_*} - \rho_*^2\left(\frac{\partial\widehat{F}[w''_{\alpha'\beta'_1}]}{\partial\eta_*} + \frac{\partial\widehat{F}[w''_{\alpha'\beta'_2}]}{\partial\eta_*}\right), \tag{A28}$$

$$d_{01} = -\frac{\partial\widehat{F}[w'_{\alpha'\beta'}]}{\partial\eta_*} + \rho_*\left(\frac{\partial\widehat{F}[w''_{\alpha'\beta'_1}]}{\partial\eta_*} + \frac{\partial\widehat{F}[w''_{\alpha'\beta'_2}]}{\partial\eta_*}\right), \tag{A29}$$

$$d_{02} = -\frac{1}{2}\frac{\partial\widehat{F}[w''_{\alpha'\beta'_1}]}{\partial\eta_*}, \tag{A30}$$

and

$$d_{11} = -\frac{\partial \widehat{F}[w''_{\alpha'\beta'_2}]}{\partial \eta_*}. \tag{A31}$$

For the case that $\rho_* = \text{constant}$,

$$\begin{aligned}\sigma_{\alpha\beta}^{\mathrm{WGC}} = C_{\mathrm{TF}} \sum_{g\neq 0} \{ & \delta_{\alpha\beta}[\rho_{\alpha'}(-\vec{g})c_{00}\rho_{\beta'}(\vec{g}) + \rho_{\alpha'+1}(-\vec{g})c_{01}\rho_{\beta'}(\vec{g}) \\ & + \rho_{\alpha'}(-\vec{g})c_{01}\rho_{\beta'+1}(\vec{g}) + \rho_{\alpha'+2}(-\vec{g})c_{02}\rho_{\beta'}(\vec{g}) \\ & + \rho_{\alpha'}(-\vec{g})c_{02}\rho_{\beta'+2}(\vec{g}) + \rho_{\alpha'+1}(-\vec{g})c_{11}\rho_{\beta'+1}(\vec{g})] \\ & + \eta_*\left(\frac{g_\alpha g_\beta}{g^2}\right)[\rho_{\alpha'}(-\vec{g})d_{00}\rho_{\beta'}(\vec{g}) + \rho_{\alpha'+1}(-\vec{g})d_{01}\rho_{\beta'}(\vec{g}) \\ & + \rho_{\alpha'}(-\vec{g})d_{01}\rho_{\beta'+1}(\vec{g}) + \rho_{\alpha'+2}(-\vec{g})d_{02}\rho_{\beta'}(\vec{g}) \\ & + \rho_{\alpha'}(-\vec{g})d_{02}\rho_{\beta'+2}(\vec{g}) + \rho_{\alpha'+1}(-\vec{g})d_{11}\rho_{\beta'+1}(\vec{g})]\}, \end{aligned} \tag{A32}$$

where

$$\begin{aligned} c_{00} = & -(\alpha' + \beta' - 1)\widehat{F}[w_{\alpha'\beta'}] + 2\rho_*(\alpha' + \beta')\widehat{F}[w'_{\alpha'\beta'}] \\ & - \rho_*^2(\alpha' + \beta' + 1)(\widehat{F}[w''_{\alpha'\beta'_1}] + \widehat{F}[w''_{\alpha'\beta'_2}]), \end{aligned} \tag{A33}$$

$$c_{01} = -(\alpha' + \beta')\widehat{F}[w'_{\alpha'\beta'}] + \rho_*(\alpha' + \beta' + 1)(\widehat{F}[w''_{\alpha'\beta'_1}] + \widehat{F}[w''_{\alpha'\beta'_2}]), \tag{A34}$$

$$c_{02} = -\frac{(\alpha' + \beta' + 1)}{2}\widehat{F}[w''_{\alpha'\beta'_1}], \tag{A35}$$

and

$$c_{11} = -(\alpha' + \beta' + 1)\widehat{F}[w''_{\alpha'\beta'_2}]. \tag{A36}$$

References

[1] C. Ravi and C. Wolverton, Acta materialia **52** 4213 (2004).
[2] K.M. Carling and E.A. Carter, Modelling and Simulation in Material Science and Engineering **11** 339 (2003).
[3] K. Osamura and T. Ogura, Metal Trans. A **15** 835 (1984).
[4] D. Hamana, A. Azizi, G. Tellouche, *et al.*, Phil. Mag. Lett. **84** 697 (2004).
[5] H. Inagaki, Zeitschrift fur metallkunke **96** 45 (2005).
[6] D. Hamana, M. Bouchear, M. Betrouche, *et al.*, J. Alloys Compounds **320** 93 (2001).
[7] D. Hamana, M. Bouchear and A. Derafa, Mater. Chem. Phys. **57** 99 (1998).
[8] C. Wolverton, Acta Materialia **49** 3129 (2001).
[9] M. Kubota, Mater. Trans. **46** 241 (2005).

[10] S.G. Corcoran, R.J. Colton, E.T. Lileodden, *et al*., Phys. Rev. B **55** 16057 (1997).
[11] W.W. Gerberich, J.C. Nelson, E.T. Lilleodden, *et al*., Acta Materialia **44** 3585 (1996).
[12] A.M. Minor, E.T. Lilleodden, E.A. Stach, *et al*., J. Electron. Mater. **31** 958 (2002).
[13] J. Knap and M. Ortiz, Phys. Rev. Lett. **90** 226102 (2003).
[14] A. Bolshakov, W.C. Oliver and G.M. Pharr, J. Mater. Res. **11** 760 (1996).
[15] C.F. Robertson and M.C. Fivel, J. Mater. Res. **14** 2251 (1999).
[16] K.J. Van Vliet, J. Li, T. Zhu, S. Yip, *et al*., Phys. Rev. B **67** 104105 (2003).
[17] S.C. Watson and E.A. Carter, Computer Phys. Commun. **128** 67 (2000).
[18] E.B. Tadmor, M. Ortiz and R. Phillips, Phil. Mag. A **73** 1529 (1996).
[19] T.J.R. Hughes, *The Finite Element Method* (Dover, New York, 2000).
[20] K. Bathe, *Finite Element Procedures* (Prentice Hall, Upper Saddle River, NJ, 1996).
[21] O.C. Zienciewics and R.L. Taylor, *The Finite Element Method*, Vol. 1–3 (Butterworth-Heinemann, 2000).
[22] J. Bonet and R.D. Wood, *Nonlinear Continuum Mechanics for Finite Element Analysis* (Cambridge University Press, Cambridge, 1997).
[23] M. Fago, R.L. Hayes, E.A. Carter, *et al*., Phys. Rev. B **70** 10010 (2004).
[24] R.L. Hayes, M. Fago, M. Ortiz, *et al*., Multiscale Modeling and Simulation **4** 359 (2005).
[25] L.M. Dupuy, E.B. Tadmor, R.E. Miller, *et al*., Phys. Rev. Lett. **95** 060202 (2005).
[26] S. Takeuchi and E. Kuramoto, Acta Metallurgica **21** 415 (1973).
[27] C. Lall, S. Chin and D.P. Pope, Metallurgical Transitions A **10** 1323 (1979).
[28] Y. Umakoshi, D.P. Pope and V. Vitek, Acta Metallurgica **32** 449 (1984).
[29] A.M. Cuitiño and M. Ortiz, Mater. Sci. Engng **A170** 111 (1993).
[30] B. Zhou, Y.A. Wang and E.A. Carter, Phys. Rev. B **69** 125109 (2004).
[31] L. Goodwin, R.J. Needs and V. Heine, J. Phys.: Condensed Matter **2** 351 (1990).
[32] S.C. Watson, B.J. Jesson, E.A. Carter, *et al*., Europhys. Lett. **41** 37 (1998).
[33] D.M. Ceperley and B.J. Alder, Phys. Rev. Lett. **45** 566 (1980).
[34] J.P. Perdew and A. Zunger, Phys. Rev. B **23** 5048 (1981).
[35] M.D. Segall, P.L.D. Lindan, M.J. Probert, *et al*., J. Physics: Condensed Matter **14** 2717 (2002).
[36] L. Wang and M.P. Teter, Phys. Rev. B **45** 13196 (1992).
[37] Y.A. Wang, N. Govind and E.A. Carter, Phys. Rev. B **58** 13465 (1998).
[38] Y.A. Wang, N. Govind and E.A. Carter, Phys. Rev. B **60** 16350 (1999).
[39] R. Hill, J. Mechan. Phys. Solids **10** 1 (1962).
[40] J.R. Rice, in *Proceedings of the 14th IUTAM Congress on Theoretical and Applied Mechanics*, edited by W.L. Koiter (North-Holland, Amsterdam, 1976), pp. 207–220.
[41] Y. Leroy and M. Ortiz, Intern. J. Numer. Analyt. Meth. Geomechanics **13** 53 (1989).
[42] D. Bigoni and T. Hueckel, Intern. J. Solids Struct. **28** 197 (1991).
[43] G.N. Wells and L.J. Sluys, in *Proceedings of the European Congress on Computational Methods in Applied Sciences and Engineering*, edited by E. Oñate, G. Bugeda and B. Suárez, ECCOMAS (CIMNE, Barcelona, Spain, 2000), CDROM.
[44] J. Li, K.J. Van Vliet, T. Zhu, *et al*., Nature **418** 307 (2002).
[45] K.L. Johnson, *Contact Mechanics* (Cambridge University Press, Cambridge, 1985).
[46] T. Zhu, J. Li, K.J. Van Vliet, *et al*., J. Mechan. Phys. Solids **52** 691 (2004).
[47] J. Li, T. Zhu, S. Yip, *et al*., Mater. Sci. Engng A **365** 25 (2004).
[48] G.S. Smith, E.B. Tadmor and E. Kaxiras, Phys. Rev. Lett. **84** 1260 (2000).
[49] Yu.N. Gornostyrev, O.Yu. Kontsevoi, A.F. Maksyutov, *et al*., Phys. Rev. B **70** 014102 (2004).
[50] B. Jesson, Simulation studies of metallic liquids and solids, D. Phil. thesis, Linacre College, Oxford (1999).
[51] O.H. Nielsen and R.M. Martin, Phys. Rev. B **32** 3780 (1985).
[52] O.H. Nielsen and R.M. Martin, Phys. Rev. B **32** 3792 (1985).
[53] B. Zhou, V. Ligneres and E.A. Carter, J. Chem. Phys. **122** 044103 (2005).
[54] P. Villars and L.D. Calvart (Editors), *Pearson's Handbook of Crystallographic Data for Intermetallic Phases* (ASM International, 1991), 2nd edn, Materials Park, OH.